JOURNAL OF THERMOPHYSICS AND HEAT TRANSFER
Vol. 20, No. 4, October–December 2006

Turbulent Flow Through a Staggered Tube Bank

You Qin Wang,[*] Peter Jackson,[†] and Timothy J. Phaneuf[‡]
University of Northern British Columbia, Prince George, British Columbia V2N 4Z9, Canada

DOI: 10.2514/1.18973

Reynolds stress model simulations of turbulent flow through a staggered tube bank were carried out using the computational fluid dynamics code FLUENT. Both wall functions and near-wall treatment approaches were used. In addition, simulations using a near-wall turbulence model, the Spalart–Allmaras turbulence model, were also carried out for comparison. Simulations were performed at a Reynolds number of 10^6 with longitudinal pitch-to-diameter ratio of 1.414 and transverse pitch-to-diameter ratio of 2.0. The primary aim was to numerically investigate the crossflow in a tube bank at a very high Reynolds number using a two-dimensional model. Reynolds stress model with both standard wall function approach and nonequilibrium wall function approach predicted the position of boundary layer separation well. The heat transfer prediction was found to be in reasonable agreement with the experimental data and the empirical correlation. Flow visualization provided a clear picture of the vortex shedding which can help us better understand the flow character. The existence of two Strouhal numbers was consistent with some experimental studies.

Nomenclature

C_f = dimensionless skin friction coefficient, $(\tau/\rho u^2)\sqrt{Re}$

C_p = mean pressure coefficient

d = tube diameter, m

$D_{T,ij}$ = turbulent diffusion, kg/s^2

f = vortex shedding frequency, 1/s

I = relative turbulence intensity, $U_{\mathrm{rms}}/V_\infty$

k = turbulent kinetic energy, m^2/s^3

Nu = local Nusselt number

P = pressure, N/m^2

Pr = Prandtl number, $\mu C_p/k$

Re = Reynolds number, $\rho V_\infty d/\mu$

T = temperature, K

u_* = friction velocity, m/s

V = velocity, m/s

V_o = reference velocity, m/s

S_L = longitudinal pitch, m

S_T = transverse pitch, m

St = Strouhal number, fd/V_∞

$\overline{u'u'}$ = Reynolds normal stress, (m/s)^2

$\overline{u'v'}$ = Reynolds shear stress, (m/s)^2

$\overline{v'v'}$ = Reynolds normal stress, (m/s)^2

Δy = distance from wall to the first grid point, m

Δy^+ = first node's wall unit, $\Delta y u_*/\nu$

ϵ = turbulent dissipation, m/s^3

ϑ = angle measured from rear stagnation, deg

κ = von Karman constant

μ = dynamic viscosity, kg/m/s

μ_t = turbulent viscosity, kg/m/s

ν = kinematic viscosity, m^2/s

ξ = vorticity magnitude $(\nabla \times \boldsymbol{V})$, 1/s

ρ = fluid density, kg/m^3

φ = angle measured from front stagnation, deg

Subscripts

f = conditions of the freestream

rms = root mean square

w = tube wall

∞ = inlet

Introduction

FLOW and heat transfer in tube bundles have many important industrial applications and have been studied in the past both experimentally and through numerical simulation. Many investigations, mostly for steady flow, have been reviewed in two earlier papers [1,2] regarding staggered tube banks and inline tube banks, respectively. A literature search on unsteady flow associated with vortex shedding in tube bundles reveals that much work has been done in the past on this subject, especially within the last decade. It was once maintained that there was insufficient space for vortices to develop in the space surrounding tube banks [3]; however, the results of flow visualization studies suggest that vortex shedding is present in tube banks. The experimental results of Abd-Rabbo and Weaver [4] showed that alternate vortex shedding occurs at low Reynolds numbers in staggered arrays. This has been confirmed recently by many flow visualization studies including Weaver et al. [5] and Price et al. [6], both using rotated square arrays. In contrast, Ziada and Oengören [7] found that inline square arrays behave quite differently; instead of alternate vortex shedding, instability in the jets between tube columns is the source of excitation. In experimental studies conducted by Oengören and Ziada [8] as well as Polak and Weaver [9], the existence of multiple Strouhal numbers has been found in normal triangular arrays. The same phenomenon has been found in rotated square arrays [5]. After a lengthy research effort, a clearer picture of the vortex shedding phenomenon is being achieved. It appears that the multiple Strouhal numbers observed in staggered tube arrays is due to alternate vortex shedding from the first few tube rows. However, a number of questions remain unanswered. There is considerable experimental evidence that a sharply defined flow periodicity, with a constant Strouhal number, does exist in some tube banks, but on the other hand, there is equally compelling experimental evidence that no flow periodicity exists for other tube banks with different geometrical patterns. It is still not clear why this phenomenon occurs in some tube banks and not in others and whether it is related to classic vortex shedding. It has been suggested [6] that flow periodicities in tube banks may be due to a number of different mechanisms rather than just one.

This paper is a follow-up of the work by Wang et al. [1,10] who had investigated laminar flow through a staggered tube bank using an in-house code as well as the CFD package FLUENT. In this paper,

---

Received 20 July 2005; revision received 22 November 2005; accepted for publication 25 February 2006. Copyright © 2006 by the American Institute of Aeronautics and Astronautics, Inc. All rights reserved. Copies of this paper may be made for personal or internal use, on condition that the copier pay the $10.00 per-copy fee to the Copyright Clearance Center, Inc., 222 Rosewood Drive, Danvers, MA 01923; include the code $10.00 in correspondence with the CCC.

[*] Senior Lab Instructor, High Performance Computing Project, College of Science and Management.

[†] Associate Professor, Environmental Science Program, College of Science and Management.

[‡] Graduate Student, Environmental Science Program, College of Science and Management.

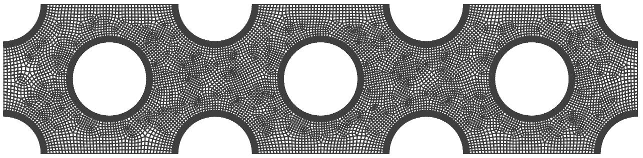

a) Coarse grid

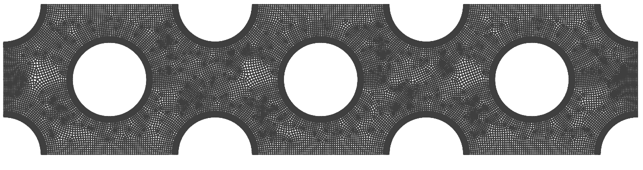

b) Fine grid

Fig. 1 Simulation domain with example grid.

we first verify that FLUENT is capable of representing low Reynolds number flow through a staggered tube bank by comparing the simulation solution with observations. The purpose is then to numerically investigate the crossflow in a tube bank at a very high Reynolds number using a 2-D turbulence model. We compared the simulation results using different wall treatments to determine which gives the most realistic result.

Simulation Overview

Numerical Approach

We started by using a 2-D Reynolds stress model (RSM) in FLUENT to simulate flow through a staggered tube bank at $Re = 1.8 \times 10^4$ and compared the results with experimental observations released through the second ERCOFTAC-IAHR Workshop of Refined Flow Modeling. After this code validation, the calculations were made for a Reynolds number of 10^6 in a tube bank arrangement with longitudinal pitch-to-diameter ratio of 1.414 and transverse pitch-to-diameter ratio of 2.0. In FLUENT calculations, wall boundaries can be treated with four different approaches: [11] 1) standard wall function (SWF), 2) nonequilibrium wall function [12], 3) near-wall treatment (viscous sublayer wall function), and 4) enhanced wall treatment (two-layer model approach). In the present study, the first three of these approaches were used and compared. In addition, simulations using the Spalart–Allmaras turbulence model [13] (referred to as "SA model" throughout), was also carried out for comparison.

Four grids were generated to be consistent with the assumptions of each wall treatment and to test for grid independence. The first grid set was created for the near-wall treatment, where the grids were clustered closely to the tube wall to ensure that the first computational node is at $y+ < 5$, and resulted in a grid with 21,682 cells. FLUENT applies the laminar stress-strain relationship that can be written as $u^+ = y^+$ for this approach. The second and the third grid sets are plotted in Fig. 1 where the coarse grid has 15,032 cells and the fine grid has 24,560 cells. These grids were created such that the first computational grid is set at $30 < y^+ < 300$ to satisfy the requirements of the standard wall function and nonequilibrium wall function approaches. In the present study, results from the fine grid were used, with the coarse grid results only used for grid-independence tests. The fourth grid set we call the "finest" grid with 46,140 cells was also used for grid independence tests (Fig. 2b).

Periodic boundary conditions were used for the inflow and outflow and a combination of periodic boundary condition with a no-slip boundary condition at the tube surfaces was used at the bottom and top boundaries. Temperature at the tube surface was 400 K and temperature at the inlet was 300 K. A segregated solution approach using the SIMPLE algorithm was used. The governing equations were discretized by the second-order upwind scheme. A second-order implicit scheme was used for the unsteady formulation. Convergence was declared when the maximum scaled residuals were less than 10^{-5} for the continuity, velocity, and temperature equations, and less than 10^{-6} for the turbulent kinetic energy equation, dissipation rate equation, and all Reynolds stress equations.

Turbulence Model

A five-equation Reynolds stress model [14–16] was used in the present study. The Reynolds stress model involves calculation of the individual Reynolds stresses, $\overline{u_i'u_j'}$, using differential transport equations. The individual Reynolds stresses are then used to obtain closure of the Reynolds-averaged momentum equation. The exact transport equations for the transport of the Reynolds stresses, $\rho\overline{u_i'u_j'}$, may be written as follows:

$$\frac{\partial}{\partial t}\rho\overline{u_i'u_j'} + C_{ij} = D_{T,ij} + D_{L,ij} + P_{ij} + G_{ij} + \phi_{ij} + \epsilon_{ij} + S_{\text{user}} \tag{1}$$

where C_{ij} is convection, $D_{T,ij}$ is turbulent diffusion, $D_{L,ij}$ is molecular diffusion, P_{ij} is stress production, G_{ij} is buoyancy production, ϕ_{ij} is pressure strain, ϵ_{ij} is dissipation, and S_{user} is user-defined source term:

$$C_{ij} \equiv \frac{\partial}{\partial x_k}(\rho u_k \overline{u_i'u_j'})$$

$$D_{T,ij} \equiv -\frac{\partial}{\partial x_k}[\rho\overline{u_i'u_j'u_k'} + \overline{p(\delta_{kj}u_i' + \delta_{ik}u_j')}]$$

$$D_{L,ij} \equiv \frac{\partial}{\partial x_k}\left[\mu\frac{\partial}{\partial x_k}(\overline{u_i'u_j'})\right] \qquad P_{ij} \equiv -\rho\left(\overline{u_i'u_k'}\frac{\partial u_j}{\partial x_k} + \overline{u_j'u_k'}\frac{\partial u_i}{\partial x_k}\right)$$

$$G_{ij} \equiv -\rho\beta(g_i\overline{u_j'\theta} + g_j\overline{u_i'\theta}) \qquad \phi_{ij} \equiv \overline{p\left(\frac{\partial u_i'}{\partial x_j} + \frac{\partial u_j'}{\partial x_i}\right)}$$

$$\epsilon_{ij} \equiv -2\mu\overline{\frac{\partial u_i'}{\partial x_k}\frac{\partial u_j'}{\partial x_k}}$$

Of the various terms in these exact equations, C_{ij}, $D_{L,ij}$, and P_{ij} do not require any modeling. However, $D_{T,ij}$, G_{ij}, ϕ_{ij}, and ϵ_{ij} need to be modeled to close the equations [17].

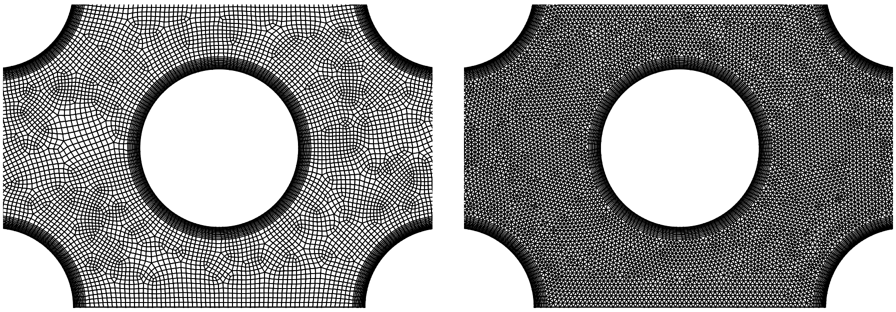

a) Fine grid b) Finest grid

Fig. 2 Details of a picture of two grid sets.

$D_{T,ij}$ can be modeled by the generalized gradient-diffusion model of Daly and Harlow [18]:

$$D_{T,ij} = C_s \frac{\partial}{\partial x_k}\left(\rho \frac{k\overline{u'_k u'_\ell}}{\epsilon}\frac{\partial \overline{u'_i u'_j}}{\partial x_\ell}\right) \tag{2}$$

However, this equation can result in numerical instabilities, so it has been simplified in FLUENT to use a scalar turbulent diffusivity as follows [19]:

$$D_{T,ij} = \frac{\partial}{\partial x_k}\left(\frac{\mu_t}{\sigma_k}\frac{\partial \overline{u'_i u'_j}}{\partial x_k}\right) \tag{3}$$

The μ_t is computed similarly to the k–ϵ models:

$$\mu_t = \rho C_\mu \frac{k^2}{\epsilon} \tag{4}$$

where $C_\mu = 0.09$.

Lien and Leschziner [19] derived a value of $\sigma_k = 0.82$ by applying the generalized gradient-diffusion model, Eq. (2), to the case of a planar homogeneous shear flow.

In FLUENT, the pressure strain term, ϕ_{ij}, in Eq. (1) is modeled using the following decomposition :

$$\phi_{ij} = \phi_{ij,1} + \phi_{ij,2} + \phi_{ij,w} \tag{5}$$

where $\phi_{ij,1}$, the slow pressure strain term, is modeled as

$$\phi_{ij,1} \equiv -C_1 \rho \frac{\epsilon}{k}\left[\overline{u'_i u'_j} - \frac{2}{3}\delta_{ij} k\right] \tag{6}$$

with $C_1 = 1.8$. $\phi_{ij,2}$, the rapid pressure strain term, is modeled as

$$\phi_{ij,2} \equiv -C_2\left[(P_{ij} - C_{ij}) - \frac{2}{3}\delta_{ij}(P - C)\right] \tag{7}$$

where $C_2 = 0.60$, P_{ij} and C_{ij} are defined as in Eq. (1), $P = \frac{1}{2}P_{kk}$ and $C = \frac{1}{2}C_{kk}$. The wall-reflection term, $\phi_{ij,w}$, is responsible for the redistribution of normal stresses near the wall. It tends to damp the normal stress perpendicular to the wall, while enhancing the stresses parallel to the wall. This term is modeled as

$$\begin{aligned}\phi_{ij,w} \equiv{}& C'_1 \frac{\epsilon}{k}\left(\overline{u'_k u'_m} n_k n_m \delta_{ij} - \frac{3}{2}\overline{u'_i u'_k} n_j n_k - \frac{3}{2}\overline{u'_j u'_k} n_i n_k\right)\frac{k^{3/2}}{C_\ell \epsilon d} \\ &+ C'_2\left(\phi_{km,2} n_k n_m \delta_{ij} - \frac{3}{2}\phi_{ik,2} n_j n_k - \frac{3}{2}\phi_{jk,2} n_i n_k\right)\frac{k^{3/2}}{C_\ell \epsilon d}\end{aligned} \tag{8}$$

where $C'_1 = 0.5$, $C'_2 = 0.3$, n_k is the x_k component of the unit normal to the wall, d is the normal distance to the wall, and $C_\ell = C_\mu^{3/4}/\kappa$, where $C_\mu = 0.09$ and $\kappa = 0.4187$.

In FLUENT, for incompressibility, the dissipation tensor ϵ_{ij} is modeled as

$$\epsilon_{ij} = \frac{2}{3}\delta_{ij}\rho\epsilon \tag{9}$$

The scalar dissipation rate ϵ is computed with a model transport equation similar to that used in the standard k–ϵ model [22]:

$$\begin{aligned}\frac{\partial}{\partial t}(\rho\epsilon) + \frac{\partial}{\partial x_i}(\rho\epsilon u_i) ={}& \frac{\partial}{\partial x_j}\left[\left(\mu + \frac{\mu_t}{\sigma_\epsilon}\right)\frac{\partial \epsilon}{\partial x_j}\right] + C_{\epsilon 1}\frac{1}{2}[P_{ii} \\ &+ C_{\epsilon 3}G_{ii}]\frac{\epsilon}{k} - C_{\epsilon 2}\rho\frac{\epsilon^2}{k} + S_\epsilon\end{aligned} \tag{10}$$

The model constants $C_{\epsilon 1}$, $C_{\epsilon 2}$, and σ_ϵ have the following default values:

$$C_{\epsilon 1} = 1.44, \qquad C_{\epsilon 2} = 1.92, \qquad \sigma_\epsilon = 1.3$$

In FLUENT, $C_{\epsilon 3}$ is not specified, but is instead calculated according to the following relation:

$$C_{\epsilon 3} = \tanh\left|\frac{v}{u}\right| \tag{11}$$

where v is the component of the flow velocity parallel to the gravitational vector and u is the component of the flow velocity perpendicular to the gravitational vector. In this way, $C_{\epsilon 3}$ will become 1 for buoyant shear layers for which the main flow direction is aligned with the direction of gravity. For buoyant shear layers that are perpendicular to the gravitational vector, $C_{\epsilon 3}$ will become zero.

Results and Discussion

Code Validation

The calculations conducted by Watterson et al. [23] and the measurements released through the second ERCOFTAC-IAHR Workshop of Refined Flow Modeling [24] were used for code validation in the present study. The experimental test section consisted of seven horizontal, staggered rows of 21.7 mm diameter rods. The Reynolds number, based on the rod diameter, was 1.8×10^4. In Watterson's study, the Reynolds-averaged Navier–Stokes equations were solved using a pressure-based finite volume algorithm, using collocated cell vertices in an unstructured and adaptive mesh of tetrahedra. Turbulence closure was obtained with a truncated form of a low-Reynolds number k–ϵ model developed by Yang and Shih [25]. Their computational domain covered all seven rows of tubes used in the experimental study. A similar arrangement with a full set of seven tubes was chosen as the computational domain in the present study (Fig. 3).

In this validation simulation we used the near-wall treatment for the wall boundary condition. Simulation results were extracted at: $x = X_i$ along AO, $x = X_r$ along CB, $y = Y_{\text{wake}}$ along CO, and $y = Y_{\text{impact}}$ along OD for comparison. The axial and transverse velocity profiles as well as the Reynolds shear stress extracted from the solution at the four transects described are plotted together with the measurements of ERCOFTAC-IAHR test case described in Simonin and Barcouda [24] and the numerical work conducted by Watterson et al. [23] in Figs. 4–6. In each figure, the results extracted at $x = X_i$, $x = X_r$, $y = Y_{\text{wake}}$, and $y = Y_{\text{impact}}$ are presented in subfigures a, b, c, and d, respectively. Because of space limitations, Reynolds normal stress of $\overline{u'u'}$ and $\overline{v'v'}$ have not been presented in this paper. Because the calculation and the experiment were performed with different fluids, a reference velocity was need to rescale the velocity and the turbulent stress for comparison. A reference velocity of 7.5 m/s, which is equal to $0.61 \times V_\infty$, was chosen by Watterson et al. that gave the best agreement between their results and measured axial velocity profiles at the transverse plane $x = X_i$. A reference velocity of 0.16 m/s, which was also obtained by $0.61 \times V_\infty$, was used in the present study in Figs. 4–6. In Fig. 4, it can be seen that overall the axial velocity profiles are well predicted, except in a small region above the tube where the axial velocity is overpredicted and in the wake region where the axial velocity is underestimated. In Fig. 5, the transverse velocity profiles are generally well predicted except in the separation region (Fig. 5b) where it is underestimated by more than 30% although the magnitude in the recirculation region is close to the expected level. The transverse velocity profiles obtained by the two numerical investigations match each other reasonably well. It should be

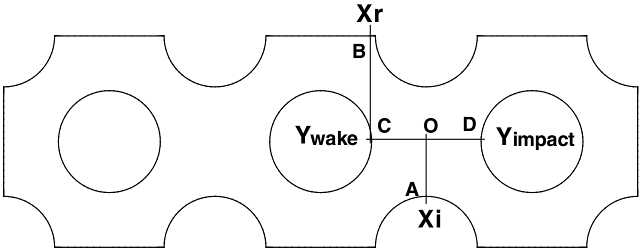

Fig. 3 Full domain for validation case, showing positions at which results were extracted.

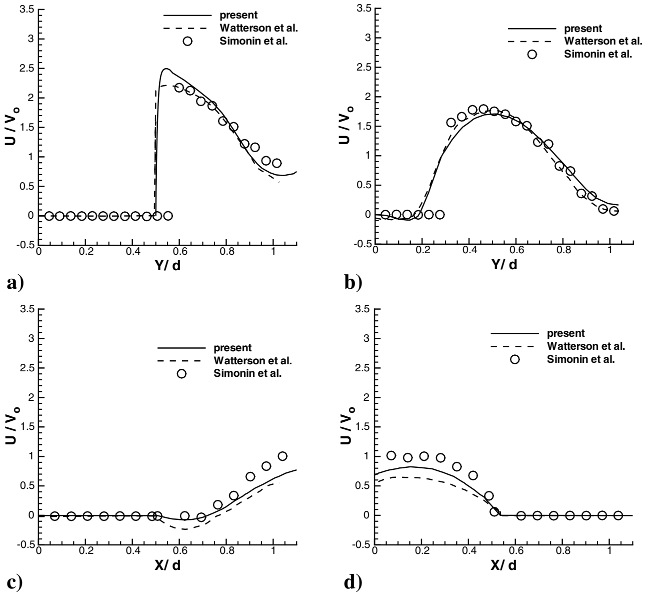

Fig. 4 Axial velocity profile: a) $x = X_i$, b) $x = X_r$, c) $y = Y_{\text{wake}}$, d) $y = Y_{\text{impact}}$.

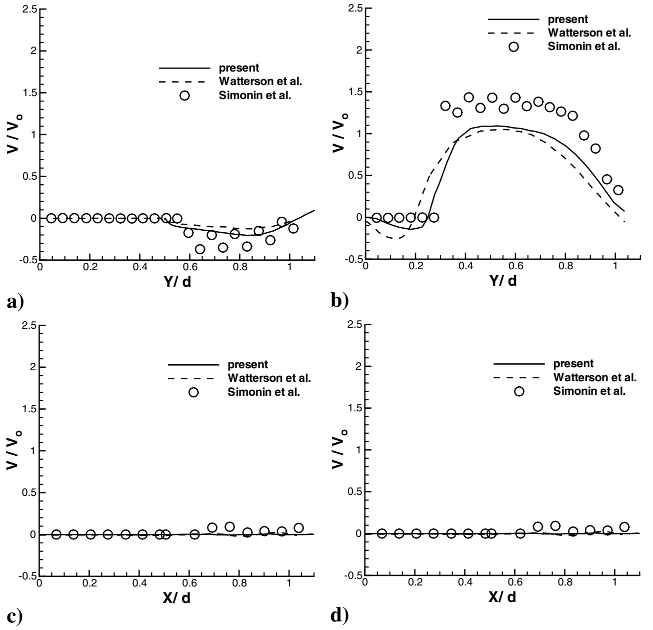

Fig. 5 Transverse velocity profile: a) $x = X_i$, b) $x = X_r$, c) $y = Y_{\text{wake}}$, d) $y = Y_{\text{impact}}$.

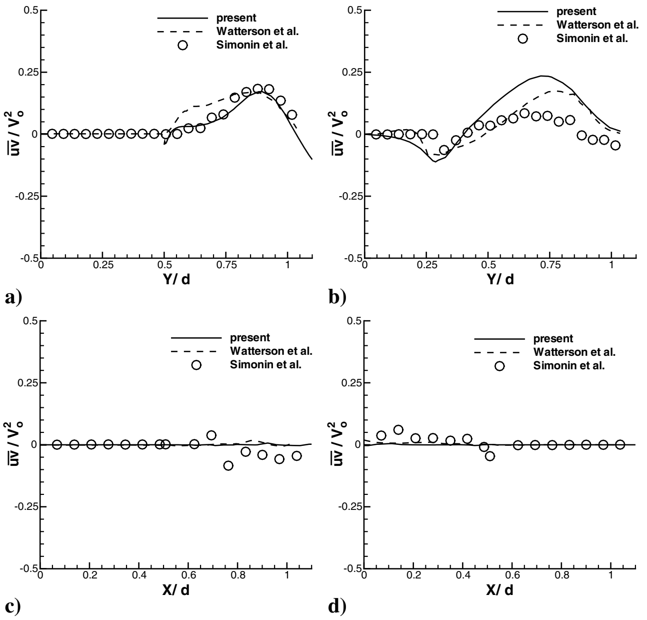

Fig. 6 Reynolds shear stress $\overline{uv}$: a) $x = X_i$, b) $x = X_r$, c) $y = Y_{\text{wake}}$, d) $y = Y_{\text{impact}}$.

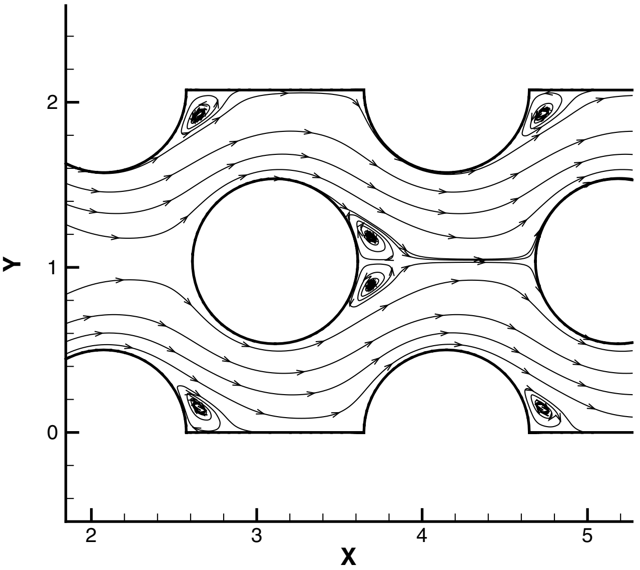

Fig. 7 Instantaneous velocity field for ERCOFTAC-IAHR test case.

mentioned that there is some uncertainty in the laser Doppler anemometry measurements [24] because zero velocity values are specified both within solid surfaces and in flow regions close to the solid walls where the measuring equipment could not access (see Figs. 4a and 4b). Reynolds shear stress $(\overline{u'v'})$ variations are well predicted in most regions, in both magnitude and trend, with the exception of the separation region where the prediction is in poor agreement with the experimental data (Fig. 6b), similar to the transverse velocity profiles. The present calculation provides a better prediction in the region above the tube (Fig. 6a).

The same ERCOFTAC-IAHR test case [24] has been computed with LES, DNS, and Reynolds stress transport model (RSTM) by Benhamadouche et al. [26] Their attempts at a 2-D RSTM simulation failed because it produced strong vortex shedding which is physically unreasonable (see Fig. 13 in their paper [26]). But both LES and 3-D RSTM resulted in improvement of the simulation in the separation region. In the present study, no vortex shedding is observed although attached eddies of recirculating flow did form behind each cylinder (Fig. 7). This plot compared well with the velocity field from the experimental result (see Fig. 2 in [24]) which indicates that a physically realistic solution was obtained in the present study by 2-D RSM. In Benhamadouche et al.'s study $D_{T,ij}$ was modeled by the generalized gradient-diffusion model of Daly and Harlow [Eq. (2)]. However, this equation can result in numerical instabilities, so it has been simplified in FLUENT to use a scalar turbulent diffusivity [Eq. (3)], as discussed in the preceding section.

Assessment of the Near-Wall Approaches

In the preceding section we have shown that the FLUENT 2-D RSM is capable of simulating flow through a staggered tube bank at $Re = 1.8 \times 10^4$ by comparing our results with simulations of Watterson et al. [23] and observations [24]. The near-wall treatment, i.e., $u^+ = y^+$ was used in that simulation. The standard wall function and nonequilibrium wall function were not successful for this low Reynolds number case because they require $30 < y^+ < 300$, which causes the first node to be too far from the tube wall. For the high

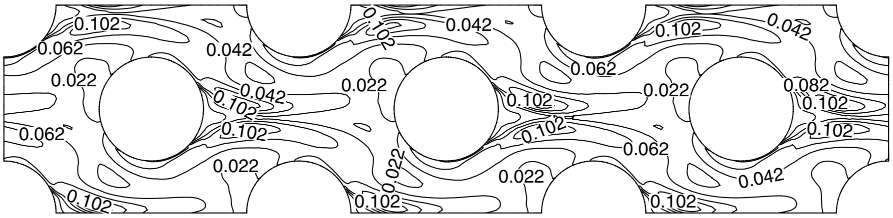

a) Standard wall function

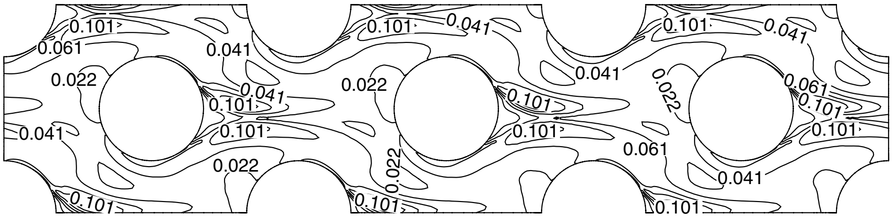

b) Non-equilibrium wall function

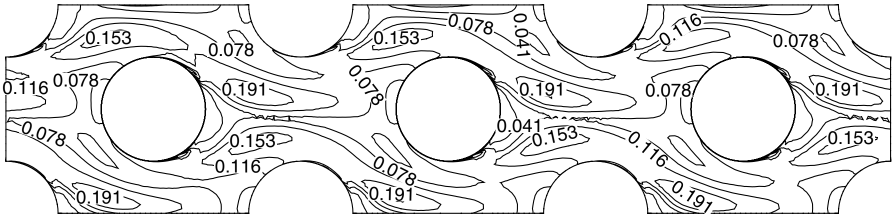

c) Near wall treatment

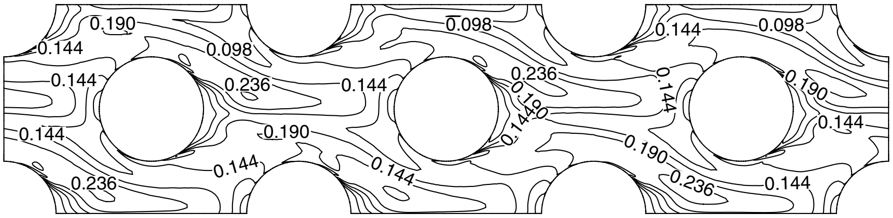

d) Near wall turbulence model

Fig. 8 Turbulence intensity ($U_{\mathrm{rms}}/V_\infty$).

Reynolds number case ($Re = 10^6$) considered in the present study, the first node is much closer to the tube wall; therefore, both the standard wall function and nonequilibrium wall function approaches were used. Four different near-wall approaches were used in the present study. They provided similar mean field predictions; however, there were differences in the magnitude of the turbulence intensity. In Fig. 8, we can see that the magnitude of the relative turbulence intensity contours obtained by the standard wall function approach and the nonequilibrium wall function approach are consistent. However, the relative turbulence intensity obtained by the near-wall treatment (Fig. 8c) and the near-wall turbulence model (SA model, Fig. 8d) are much higher than those obtained using the other two approaches. The peak value of relative turbulence intensity obtained by the near-wall treatment was 34% and by the SA model was 28%. The relative turbulence intensity obtained by the SA model and the near-wall treatment seems physically unrealistic as values this high are seldom reported. The determination of physically unrealistic simulations using the SA model and the near-wall treatment is not only based on these peak turbulence intensity values, but also based on other predictions such as mean heat transfer (this is discussed in a later section). Although a value of 35% was previously reported [26] in a staggered tube bank simulation, it is not clear how the turbulence intensity was defined in that study.

Flow and Temperature Predictions

Mean velocity, static temperature, and rms velocity extracted from the solution at two of four stations described in the code validation section are plotted in Figs. 9–13. Solutions obtained by RSM with SWF with the fine grid and two different time steps, $\mathrm{d}t = 0.001$ s and $\mathrm{d}t = 0.005$ s are practically identical. The differences among solutions obtained by three grid sets (coarse, fine, finest) is difficult to detect, except in the separation region. In the separation region, fine grid and finest grid solutions are very similar, except in 12b. But a clear discrepancy can be found between solutions obtained by the coarse grid and the fine grid, for example, in the mean transverse velocity profile, mean static temperature distribution, as well as rms of mean velocity profiles. From the distribution of skin friction and the mean pressure coefficient around the tube plotted in the later section, we know the flow separation point is at $\varphi = 146$ deg. Because of the very hot fluid separating from the tube, a maxima can be found in the temperature distribution near $y/d \approx 1.2$ in Fig. 11. For the coarse grid, a slight delay in the separation location causes the maxima to move toward the tube centerline. Separation also causes

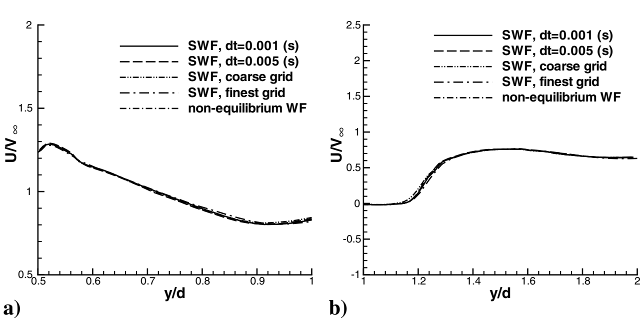

Fig. 9 Mean axial velocity profile: a) $x = X_i$, b) $x = X_r$.

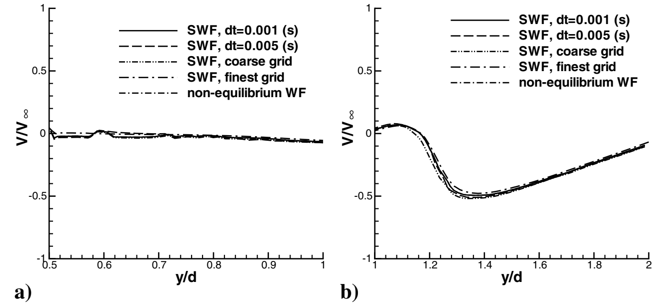

Fig. 10 Mean transverse velocity profile: a) $x = X_i$, b) $x = X_r$.

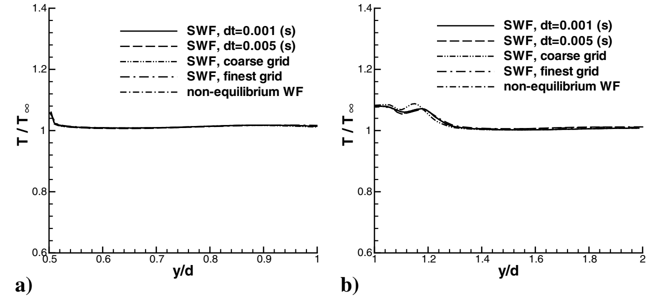

Fig. 11 Mean temperature profile: a) $x = X_i$, b) $x = X_r$.

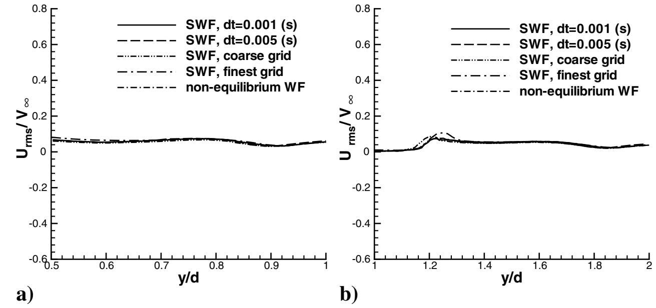

Fig. 12 Root mean square axial velocity profile: a) $x = X_i$, b) $x = X_r$.

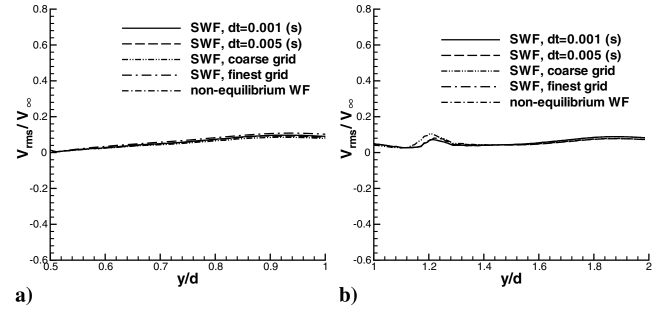

Fig. 13 Root mean square transverse velocity profile: a) $x = X_i$, b) $x = X_r$.

high turbulence intensity, which is why a maxima at the same location can be found in both the U_{rms} and V_{rms} distributions. In the case studied, because there is no obvious difference among solutions obtained with $\mathrm{d}t = 0.001$ s and $\mathrm{d}t = 0.005$ s, this indicates that a time step of 0.001 s, used in the present study, is small enough to resolve the flow features. In the present study, mean velocities were averaged among 6000 samples which correspond to 48 vortex shedding cycles.

Statistical Features for Unsteady Flow

Part of the temporal evolution of the streamwise drag force coefficient and the frequency spectra of the streamwise drag coefficient are shown in Figs. 14 and 15, respectively. The simulation

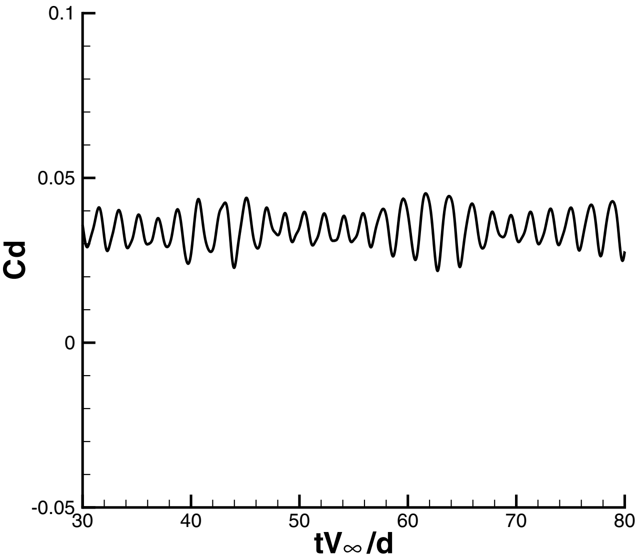

Fig. 14 Temporal evolution of the streamwise drag force coefficient around the center tube.

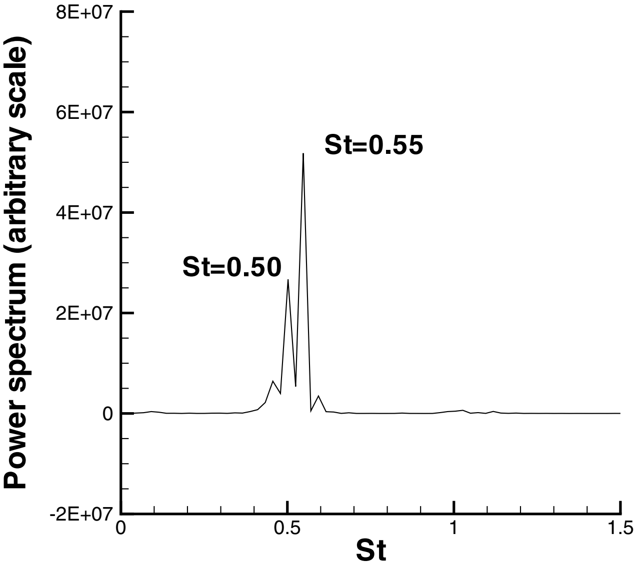

Fig. 15 Power spectra of the streamwise drag coefficient.

results shown were taken downstream of the fifth tube row, i.e., the center tube. In Fig. 15, the frequency has been converted to a Strouhal number. Two spectral peak values were obtained in the present study. The higher peak was 0.55, which correspond to $f = 8.031/\mathrm{s}$, i.e., it took approximately 0.12 s to complete a whole vortex shedding cycle. The value estimated from flow visualization discussed in the following section is 0.12 s, which matches very well with the main peak value obtained by statistical analysis. It is not clear what causes the second peak. The existence of multiple Strouhal numbers for certain normal triangular tube arrays has been known for some time. For example, two Strouhal numbers were found by Polak and Weaver [9] in normal triangular arrays for $S_D/d \geq 2$. Their experimental results indicated that the multiple Strouhal number observed in normal triangular tube arrays is due to alternate vortex shedding from the first few tube rows resulting in a high-frequency flow fluctuation, whereas a low-frequency fluctuation was caused by second-row vortex shedding. Oengören and Ziada [8] also studied the vortex shedding phenomena in normal triangular arrays and observed two different Strouhal numbers that stemmed from different vortex shedding frequencies in the front and inner rows. They found that the high-frequency component was associated with alternating vortex shedding from the front rows, and a low-frequency

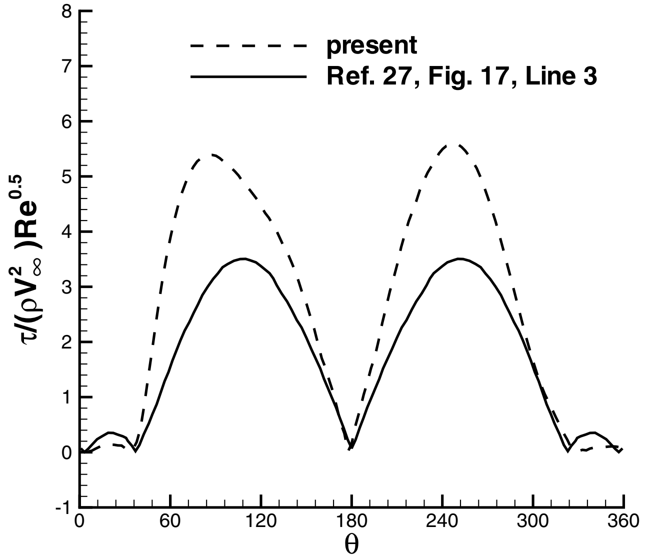

Fig. 16 Distribution of the instantaneous skin friction coefficient $C_f = (\tau/\rho u^2)\sqrt{Re}$ over the tube.

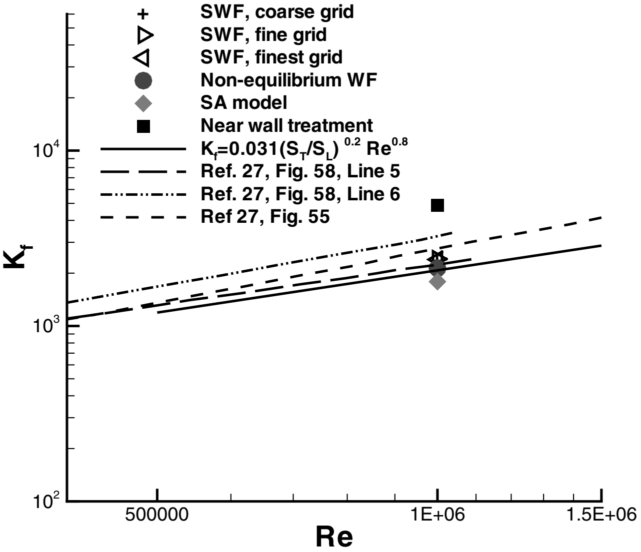

Fig. 17 Mean heat transfer.

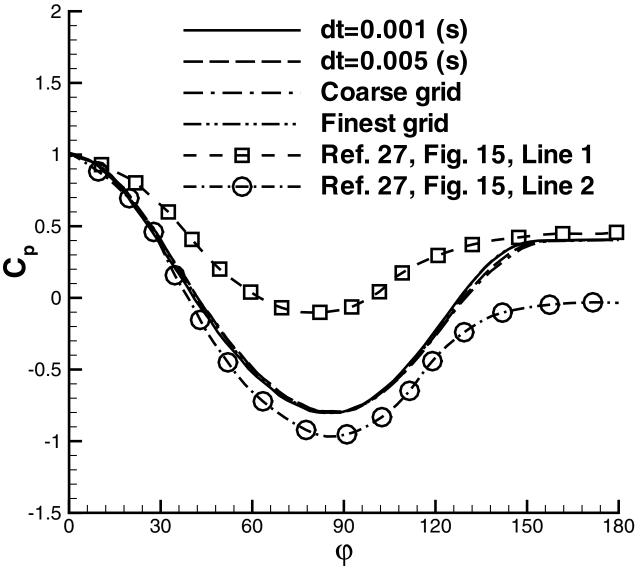

Fig. 18 Mean pressure coefficient.

component was associated with alternating vortex shedding from the rear rows. They also noted that for high Reynolds number and intermediate pitch ratios ($S_D/d = 2.08$) the low-frequency component dominated the entire array.

In previous experimental studies, a wide range of Strouhal number has been found. We believe that the wide range of Strouhal number may be due to difference in the locations chosen to measure the flow, as well as flows of different Reynolds number in each study. In a previous investigation conducted by Weaver et al. [5], it has been found that experimental observations of vortex shedding in tube arrays are strongly dependent on row depth and Reynolds number. Polak and Weaver's model [9] was only four tube rows deep and three columns wide, and the two Strouhal numbers obtained from their experimental study were 0.855 and 0.544. Oengören and Ziada's model [8] was ten tube rows deep and ten columns wide, and the two Strouhal numbers obtained from their experimental study were 0.40 and 0.28. The present study investigated the deep inner tube arrays at $Re = 10^6$, and we obtained two values of 0.55 and 0.50.

Wall Friction and Pressure Distributions

The instantaneous skin friction coefficient around the tube obtained by RSM with SWF is plotted in Fig. 16. Note that the skin friction coefficient C_f is made dimensionless using $C_f = (\tau/\rho u^2)\sqrt{Re}$, to compare our results with the experimental observation of Achenbach cited in Žukauskas [27] Fig. 17. Achenbach conducted an experiment with a longitudinal pitch-to-diameter ratio of 1.4 and transverse pitch-to-diameter ratio of 2 at $Re = 1.4 \times 10^6$. His results indicate that the separation point is around $\varphi = 145$ deg. For simulation using RSM with SWF approach, the average of the top and bottom half tube separation angle gives $\varphi = 146$ deg which is in good agreement with Achenbach's data. It is obvious that the present study overpredicted the skin friction coefficient by more than 30% compared with the experimental result (Fig. 16). This may be because our tubes are heated. There is no temperature information provided with Achenbach's experimental data. However, in Žukauskas [27] Fig. 6, a definite influence of heating on frictional drag can be noted. The maximum of C_f with $\Delta T \approx 50\,^\circ\mathrm{C}$ is about 16% higher than that with $\Delta T = 0$. In the present study, ΔT was 100 K.

Mean heat transfer values averaged around the tube, along with the experimental data and the empirical correction are plotted in Fig. 17. Here K_f is defined by

$$K_f = Nu_f Pr_f^{-0.36}(Pr_f/Pr_w)^{-0.25} \tag{12}$$

and for gaseous flows when $Pr_f = 0.7$

$$K_f = 1.137 Nu_f \tag{13}$$

The empirical correlation used in Fig. 17 is for the heat transfer in the inner rows of staggered banks at $Re > 2 \times 10^5$ suggested by Žukauskas [27]:

$$Nu_f = 0.031(S_T/S_L)^{0.2} Re^{0.8} Pr_f^{0.4}(Pr_f/Pr_w)^{0.25} \tag{14}$$

and for gaseous flows when $Pr_f = 0.7$

$$Nu_f = 0.027(S_T/S_L)^{0.2} Re^{0.8} \tag{15}$$

The experimental data plotted in Fig. 17 are from Žukauskas [27] Fig. 58, Line 5 for $S_T \times S_L = 1.6 \times 1.4$, Line 6 for $S_T \times S_L = 2.1 \times 1.4$, and Fig. 55 for $S_T \times S_L = 2.0 \times 1.25$.

It is evident from Fig. 17 that, in the case studied, the RSM with near-wall treatment provided an unrealistic prediction for heat transfer, the SA model provided a underprediction of heat transfer, and only RSM with SWF and RSM with nonequilibrium wall function provided a heat transfer which is comparable with the experimental data and the empirical correlation.

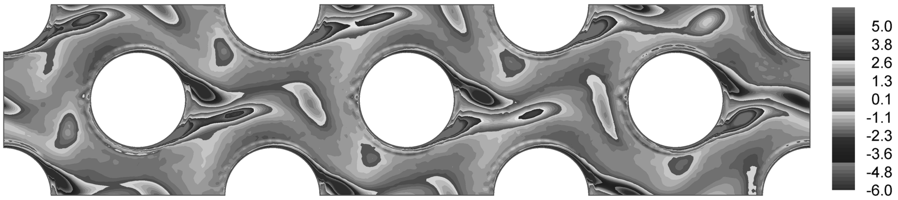

a) $t = 6.0097$ **(*s*)**

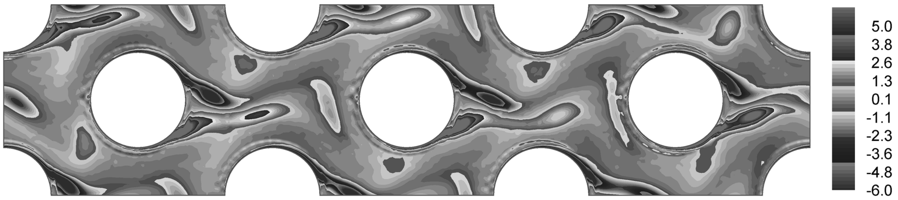

b) $t = 6.0297$ **(*s*)**

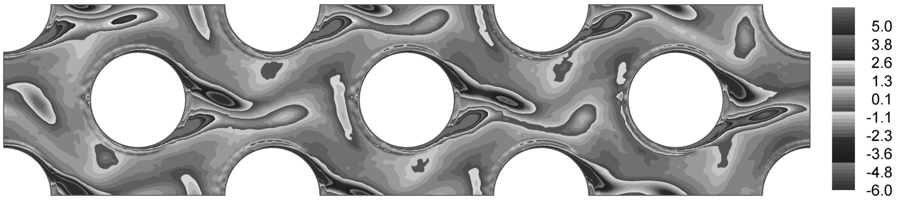

c) $t = 6.0497$ **(*s*)**

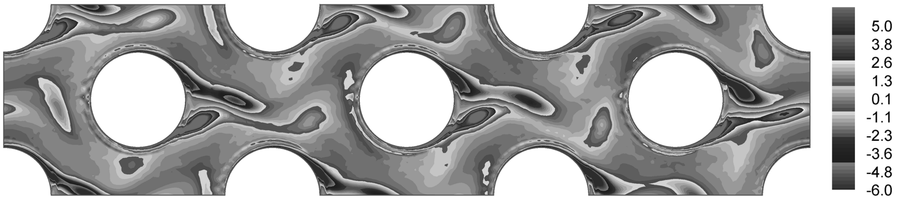

d) $t = 6.0697$ **(*s*)**

Fig. 19 Temporal evolution of vorticity ($\xi d/V_\infty$).

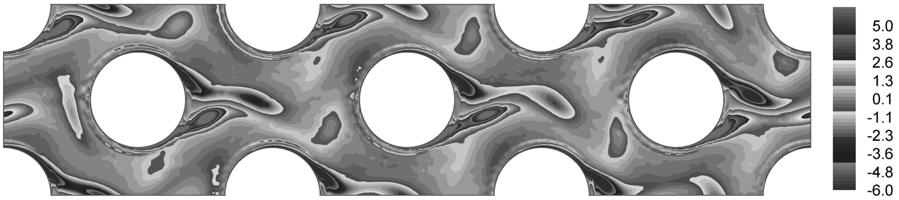

a) $t = 6.0897$ **(*s*)**

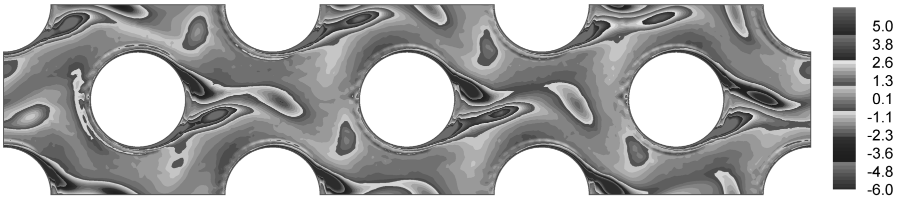

b) $t = 6.1097$ **(*s*)**

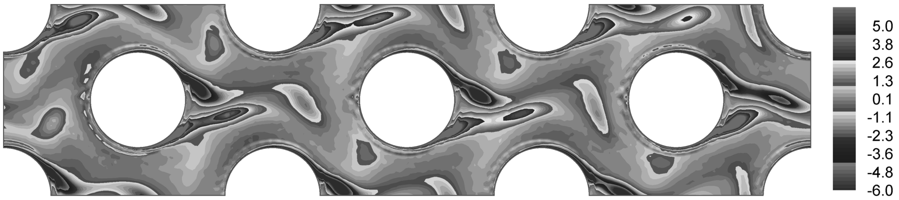

c) $t = 6.1297$ **(*s*)**

Fig. 20 Temporal evolution of vorticity, continued ($\xi d/V_\infty$).

Distributions of mean pressure coefficient C_p over the tube from our simulating are plotted with Achenbach's experimental data [27] in Fig. 18. The first line and the second line represent the distribution of the pressure coefficient on a tube in the second row and the fourth row from Achenbach at $Re = 1.5 \times 10^6$. No information about longitudinal pitch-to-diameter ratio and transverse pitch-to-diameter ratio was available for the experimental results. Solutions obtained by RSM with SWF using different grids and different time steps are very similar with each other and fall between the two experimental lines. This again indicates that a grid-independent solution has been achieved in the present study. Consistent with the C_f, the separation location has been well predicted in the mean pressure coefficient distribution. Overall, the present study predicted mean pressure coefficient reasonably well in the front tube part, but has a higher value in the rear tube part, compared with the experimental results.

Flow Visualizations

Figures 19 and 20 present the evolution of the vorticity fields around the tube from $t = 6.0097$ s to $t = 6.1297$ s and clearly capture the character of the vortex shedding. We will discuss the evolution of the vortex around the center tube only. The sequence begins in Fig. 19a with a concentration of positive vorticity that has just detached from the lower surface of the center tube. A new vortex has already started to form on the lower surface of the tube. The detached vortex is elongated as the flow is accelerated through the gap between the tubes of the next row. While this detached vortex is stretched and moved downstream, the vortex which is still attached to the upper surface of the tube continues to grow until it is finally shed; see Figs. 19b–19d. At the same time, the vortex which has already formed on the lower surface of the tube continues to grow. Finally, when this vortex grows too large to remain attached to the tube, it is shed (see Figs. 20a and 20b). Figure 20c is similar to Fig. 19a, as the flow starts a new vortex shedding cycle. Abd-Rabbo and Weaver [4] have found that there was no evidence of vortices surviving past the downstream tube in their experimental study in a rotated square array of flexible tubes with a pitch-to-diameter ratio of 1.41. However, it can be seen from Figs. 19 and 20 that the vortices previously shed from the lower side of the tubes in row two are squeezed and reduced in size when passing the gap between tubes in row three and in row four, but can still be distinguished. They are stretched when passing the gap of tubes between row three and four, and merge with the vortices formed in the lower side of the tubes in row four. At the same time, vortices shed from the upper side of the tubes in row two are always smeared out into the front wall of the tubes in row four.

Conclusions

First, the results of comparison with an established ERCOFTAC-IAHR test case [24] indicated that a physically realistic solution for turbulent flow in a staggered tube bank can be obtained by FLUENT using a 2-D Reynolds stress model. Next, the calculation of high Reynolds number turbulent flow in a staggered tube bank was presented. RSM with both SWF approach and nonequilibrium wall function approach predicted the position of boundary layer separation well. The heat transfer prediction obtained by RSM with SWF and RSM with nonequilibrium was found to be in reasonable agreement with the experimental data and the empirical correlation. The skin friction coefficient was not predicted as accurately compared to the experimental data. A possible reason for the discrepancy was that simulation and experiment have different temperature differing between the tube and air. Flow visualization provided a clear picture of the vortex shedding which can help us better understand the flow character. The existence of two Strouhal numbers was consistent with some experimental studies. Overall, the agreement between the predictions and experiments was encouraging and the present study gave confidence in the 2-D RSM for high Reynolds number turbulent flow in a staggered tube bank.

Acknowledgments

Computing infrastructure for this work was provided by grants from Canada Foundation for Innovation, British Columbia Knowledge Development Fund, SGI Canada, and donors to University of Northern British Columbia (Project number: 1854; Institute: University of Northern British Columbia). Simulations were performed on an SGI Origin 3400 with 28 processors.

References

[1] Wang, Y. Q., Penner, L. A., and Ormiston, S. J., "Analysis of Laminar Forced Convection of Air for Crossflow in Banks of Staggered Tubes," *Numerical Heat Transfer, Part A, Applications*, Vol. 38, No. 8, 2000, pp. 819–845.

[2] El-Shaboury, A. M. F., and Ormiston, S. J., "Analysis of Laminar Forced Convection of Air Crossflow in In-Line Tube Banks with Nonsquare Arrangements," *Numerical Heat Transfer, Part A, Applications*, Vol. 48, No. 1, 2005, pp. 99–126.

[3] Owen, P. R., "Buffeting Excitation of Boiler Tube Vibration," *Journal of Mechanical Engineering Science*, Vol. 7, No. 4, 1965, pp. 431–439.

[4] Abd-Rabbo, A., and Weaver, D. S., "A Flow Visualization Study of Flow Development in a Staggered Tube Array," *Journal of Sound and Vibration*, Vol. 106, No. 2, 1986, pp. 241–256.

[5] Weaver, D. S., Lian, H. Y., and Huang, X. Y., "Vortex Shedding in Rotated Square Arrays," *Journal of Fluids and Structures*, Vol. 7, No. 2, 1993, pp. 107–121.

[6] Price, S. J., Paidoussis, M. P., and Mark, B., "Flow Visualization of the Interstitial Cross-Flow Through Parallel Triangular and Rotated Square Arrays of Cylinders," *Journal of Sound and Vibration*, Vol. 181, No. 1, 1995, pp. 85–98.

[7] Ziada, S., and Oengören, A., "Vortex Shedding in an In-line Tube Bundle with Large Spacings," *Journal of Fluids and Structures*, Vol. 7, No. 6, 1993, pp. 661–687.

[8] Oengören, A., and Ziada, S., "An In-Depth Study of Vortex Shedding Acoustic Resonance and Turbulent Forces in Normal Triangle Tube Arrays," *Journal of Fluids and Structures*, Vol. 12, No. 6, 1998, pp. 717–758.

[9] Polak, D. R., and Weaver, D. S., "Vortex Shedding in Normal Triangular Tube Arrays," *Journal of Fluids and Structures*, Vol. 9, No. 1, 1995, pp. 1–17.

[10] Wang, Y. Q., "Laminar Flow Through a Staggered Tube Bank," *Journal of Thermophysics and Heat Transfer*, Vol. 18, No. 4, 2004, pp. 557–559.

[11] *FLUENT 6.0 User's Guide*, Fluent, Inc., Lebanon, NH, 2001, Chap. 10, Sec. 8.

[12] Launder, B. E., and Spalding, D. B., "The Numerical Computation of Turbulent Flows," *Computer Methods in Applied Mechanics and Engineering*, Vol. 3, No. 2, 1974, pp. 269–289.

[13] Spalart, P. R., and Allmars, S. R., "A One-Equation Turbulence Model for Aerodynamic Flows," *La Recherche aerospatiale : bulletin bimestriel de l'Office national d'etudes et de recherches aerospatiales*, Vol. 1, No. 1, 1994, pp. 5–21.

[14] Gibson, M. M., and Launder, B. E., "Ground Effects on Pressure Fluctuations in the Atmospheric Boundary Layer," *Journal of Fluid Mechanics*, Vol. 86, No. 3, 1978, pp. 491–511.

[15] Launder, B. E., "Second-Moment Closure: Present… and Future?," *International Journal of Heat and Fluid Flow*, Vol. 10, No. 4, 1989, pp. 282–300.

[16] Launder, B. E., Reece, G. J., and Rodi, W., "Progress in the Development of a Reynolds-Stress Turbulence Closure," *Journal of Fluid Mechanics*, Vol. 68, No. 3, 1975, pp. 537–566.

[17] *FLUENT 6.0 User's Guide*, Fluent, Inc., Lebanon, NH, 2001, Chap. 10, Section 6.

[18] Daly, B. J., and Harlow, F. H., "Transport Equations in Turbulence," *Physics of Fluids*, Vol. 13, No. 9, 1970, pp. 2634–2649.

[19] Lien, F. S., and Leschziner, M. A., "Assessment of Turbulent Transport Models Including Non-Linear RNG Eddy-Viscosity Formulation and Second-Moment Closure," *Computers and Fluids*, Vol. 23, No. 8, 1994, pp. 983–1004.

[20] Fu, S., Launder, B. E., and Leschziner, M. A., "Modeling Strongly Swirling Recirculating Jet Flow with Reynolds-Stress Transport Closures," *Proceedings of the Sixth Symposium on Turbulent Shear Flows*, Univ. of Toulouse, Toulouse, France, 1987, pp. 17.6.1–17.6.6.

[21] Launder, B. E., "Second-Moment Closure and Its use in Modeling Turbulent Industrial Flows," *International Journal for Numerical Methods in Fluids*, Vol. 9, No. 8, 1989, pp. 963–985

[22] Launder, B. E., and Spalding, D. B., *Lectures in Mathematical Models of Turbulence*, Academic Press, London, 1972.

[23] Watterson, J. K., Dawes, W. N., Savill, A. M., and White, A. J., "Prediction Turbulent Flow in a Staggered Tube Bundle," *International Journal of Heat and Fluid Flow*, Vol. 20, No. 6, 1999, pp. 581–591.

[24] Simonin, O., and Barcouda, M., "Measurements and Prediction of Turbulent Flow Entering a Staggered Tube Bundle," *Proceedings of the Fourth International Symposium on Applications of Laser Anemometry to Fluid Mechanics*, Lisbon, 1988.

[25] Yang, Z., and Shih, T. H., "A k–ϵ Model for Turbulent and Transitional Boundary Layers," *Near Wall Turbulent Flows*, edited by R. M. C. So, C. G. Speziale, and B. M. Launder, Elsevier, Amsterdam, 1993, pp. 165–176.

[26] Benhamadouche, S., and Laurence, D., "LES, Course LES, and Transient RANS Comparisons on the Flow Across a Tube Bundle," *International Journal of Heat and Fluid Flow*, Vol. 24, No. 4, 2003, pp. 470–479.

[27] Žukauskas, A., "Heat Transfer from Tubes in Crossflow," *Advances in Heat Transfer*, Vol. 18, No. 1, 1987, pp. 87–159.